REVISION 1: Spinel-rich lithologies in the lunar highland crust: Linking lunar samples with crystallization experiments and remote sensing.

Juliane Gross[1,3], Peter J. Isaacson[2], Allan H. Treiman[3], Loan Le[4], and Julia K. Gorman[3,*]

[1]American Museum of Natural History, New York NY 10024, jgross@amnh.org

[2]University of Hawaii (HIGP/SOEST), Honolulu HI 96822

[3]Lunar and Planetary Institute, Houston TX 77058

[4]Jacobs Technology, JETS - JSC Engineering, Technology and Science, Houston TX 77058

[*]now at University of Maryland, College Park MD 20742

Abstract:

Mg-Al spinel is rare in lunar rocks (Apollo and meteorite collections), and occurs mostly in troctolites and troctolitic cataclastites. Recently, a new lunar lithology, rich in spinel and plagioclase, and lacking abundant olivine and pyroxene, was recognized in visible to near-infrared (VNIR) reflectance spectra by the M^3 instrument on the Chandrayaan-1 spacecraft at the Moscoviense basin. These outcrop-scale areas are inferred to contain 20-30 % Mg-Al spinel. Possible explanations for the petrogenesis of spinel-bearing and spinel-rich lithology(s) range from low-pressure near-surface crystallization to a deep-seated origin in the lower lunar crust or upper mantle. Here, we describe 1-bar crystallization experiments conducted on rock compositions rich in olivine and plagioclase that crystallize spinel. This would be equivalent to impact-melting, which is moderately common among lunar plutonic rocks and granulites. To explore possible precursor materials and the maximum amount of spinel that could be crystallized, a lunar troctolitic composition similar to Apollo pink spinel troctolite 65785, and a composition similar to ALHA81005 as analogue to the source region of this meteorite have been chosen. The crystallization experiments on the composition of AHLA 81005 did not yield any spinel; experiments on the composition similar to Apollo 65785 crystallized a maximum of ~8 wt% spinel, much less than the suggested 20-30 % spinel of the new lithology detected by M^3. However, our VNIR spectral reflectance analyses of the experimental run products indicate that the spinel composition of the experimental run products not only appears to be similar to the composition of the spinel lithology detected by M^3 (characteristics of the spinel absorption), but also that the modal abundances of coexisting phases (e.g., mafic glass) influence the spectral reflectance properties. Thus, the spinel-rich deposits detected by M^3 might not be as spinel-rich as previously thought and could contain as little as 4-5 wt% spinel. However, the effect of space weathering on spinel is unknown and could significantly weaken its 2 μm absorptions. If this occurs, weathered lunar rocks could contain more spinel than a comparison with our unweathered experimental charges would suggest.

Key words: Lunar, pink spinel, M^3, V/NIR reflectance spectra, crystallization experiments, spinel-rich lithologies, remote sensing, Apollo 65875.

INTRODUCTION:

The lunar crust preserves some of the most important clues to the Moon's history and its chemical evolution (e.g., Taylor 1982; Shearer and Papike 1999; Wieczorek et al. 2006; Demidova et al. 2007; Isaacson et al. 2011). Among fragments of the lunar crust that have been returned as samples and meteorites are a few that contain Mg-Al spinel, $(Mg,Fe)Al_2O_4$. In the last few years, regions rich in Mg-Al spinel have been detected by the

Moon Mineralogy Mapper (M^3), the near-infrared (NIR) mapping spectrometer on the Chandrayaan-1 spacecraft (e.g., Pieters et al. 2010, 2011; Lal et al. 2011) which has renewed the debate on the origin of lunar highlands and the interest in spinel-bearing rocks and lithologies on the Moon (e.g., Prissel et al. 2012, 2013; Gross and Treiman 2011, Gross et al. 2011; Pieters et al. 2010, 2011; Lal et al. 2011). These areas now include portions of the Moscoviense basin, the Thompson/Ingenii basins (Pieters et al. 2011, 2013), the Theophilus crater (Dhingra et al. 2011, Lal et al. 2011), the Tycho crater (Kaur et al. 2012), and the Copernicus crater (Dhingra et al. 2013). Most of these deposits are inferred to be rich in $(Mg,Fe)Al_2O_4$ spinel (hereafter called spinel) and plagioclase (or plagioclase-composition glass), with less than 5% mafic silicate minerals, i.e., olivine and pyroxene (Pieters et al. 2011). Pieters et al. (2010, 2011) suggested that these deposits could represent a previously unknown lunar rock type, a pink spinel anorthosite (PSA).

Few lunar samples contain spinel, and those that do are mostly troctolites (olivine-plagioclase rich rocks) and cataclasites (brecciated rocks) (Table 1). However, of these spinel-bearing samples, only two contain more than ~5-6% spinel: a spinel-troctolite in 67435 which contains ~13 vol% spinel, among olivine, plagioclase and metal (Prinz et al. 1973; Warner et al. 1976; Ma et al. 1981); and a unique fragment of spinel-anorthositic troctolite in the meteorite ALHA81005 that contains ~30 vol% $(Mg,Fe)Al_2O_4$ spinel, among plagioclase and ~20 vol% olivine and pyroxene (Gross et al. 2011; Gross and Treiman 2011). Thus, spinel-bearing/rich rocks such as PSA might be an important component of the lunar crust and it is important to account for their petrogenesis in the early crust especially as spinel could indicate high-pressure formation or unusual igneous fractionations (Longhi and Boudreau 1979; Morgan et al. 2006).

Possible explanations for their petrogenesis range from low-pressure near-surface crystallization to a deep-seated origin in the lower lunar crust or upper mantle (Table 1); four major hypotheses have been offered. These proposed hypotheses are:

(1) *Spinel formed at low pressure from melts of unusual composition, rich in olivine and plagioclase components such as might be formed from an impact-melted troctolite or troctolitic anorthosite* (Treiman et al. 2010). Liquidus equilibria in simple systems show that bulk rock compositions rich in olivine + plagioclase components will produce melts that crystallize spinel (Walker et al. 1979b). Low-pressure experiments on natural Apollo samples indicate that such compositions could be produced by partial or complete melting of lunar crustal materials, and not necessary by partial melting of material from the deep inside the Moon (Walker et al. 1973b). This would be equivalent to impact-melting of troctolitic rocks, which is moderately common among lunar plutonic rocks and granulites; in this hypothesis, spinel-bearing rocks were formed from olivine-plagioclase melts produced by impact melting on or near the surface (Marvin and Walker 1985; Walker 1983). This scenario was confirmed by low-pressure experiments on plagioclase-olivine melting rates (Marvin and Walker 1985) from natural samples. On the other hand, spinel-rich rocks could be restites, residuals after a basaltic melt was removed from a partially melted rock rich in olivine and plagioclase (Taylor and Bence 1975; see Marvin et al. 1989).

There is considerable current interest in the chemical compositions of lunar impact melts and the products of their differentiation (e.g., Dhingra et al. 2013; Hurwitz and Kring, 2013; Vaughan et al. 2013). The compositions of lunar impact melts and their differentiation products obviously depend on what portions of the moon were melted in each event, and retained in the crater.

(2) *Spinel formed at low pressure by chemical reaction between picritic magma and crustal anorthositic wall-rock* (Finnila et al. 1994; Morgan et al. 2006; Gross and Treiman 2011). In this case, lunar spinel-rich areas represent the reaction zones between crust and picritic magma, and have been excavated from the crust by the adjacent impact basins and craters. Based on the petrography and mineral chemistry of a spinel-rich clast in ALHA81005 Gross and Treiman (2011) suggested that this rock type (similar to the PSA on the lunar surface) formed from a picritic magma that assimilated crustal anorthosite at low pressures.

(3*) Spinel formed at high pressure in the deep crust (deeper than ~60 km), from basaltic or peridotitic precursors, thus, the spinel-rich areas represent deep crust excavated by impacts* (Herzberg 1978; Herzberg and Baker 1980; Baker and Herzberg 1980). In this mechanism, spinel-formation depends solely on high pressure, analogous to the transition from plagioclase- to spinel-lherzolites in the Earth. However, in chemical systems that represent basalts and peridotites, the stability field of spinel enlarges as pressure increases, to the point that, at >1 GPa, olivine cannot coexist with plagioclase (e.g., Walker et al. 1973a; Longhi 1978; Soulard et al. 1994). High pressure investigations on liquidus phase-relations of natural Apollo highland rocks showed that these compositions do not represent magmas derived by partial melting of differentiated source regions at any pressure in the Moon (Delano 1977).

(4) Spinel formed during assimilation of anorthosite wall-rock by basaltic magmas at intermediate pressures, >0.5 GPa, >10 km depth (Prissel et al. 2012, 2013). This

mechanism is a hybrid of mechanisms (2) and (3) above, recognizing that spinel formation from 'basaltic magma' + anorthite is affected both by ambient pressure and by normative olivine content of the magma. At low pressures, spinel can form by reaction of plagioclase with magmas of high normative olivine (i.e., picrites); at higher pressures, the field of spinel stability expands, and permits spinel to form during interaction of anorthite and more normal (not picritic) basalts (Prissel et al. 2012, 2013). Similarly, the spinel liquidus field is more restricted for ferroan basalt compositions than for magnesian compositions, so that ferroan spinels should (in theory) tend to form at higher pressures than magnesian spinels.

Clearly, there is no consensus on the petrogenesis of highlands spinel-bearing/spinel-rich rocks. Do they represent deep-crustal material excavated by an impact, are they reaction zones at the edges of mafic intrusions into the anorthositic crust, or do they represent crystallized material from an impact melt sheet?

Here, we report on 1-bar crystallization experiments (as analogues for impact melt crystallization) on (1) a lunar troctolitic composition similar to the Apollo pink spinel troctolite 65785 that represent an analogue for a precursor surface material melted in an impact event, and (2) a composition similar to ALHA81005 that represent an analogue for the source region composition of this meteorite that would have been melted in an impact event. We explore the maximum amount of spinel that could be crystallized during an impact event and place constraints on the formation of spinel-rich lithologies. Further, we compare reflectance spectra of the experimental run products to the reflectance spectra of the spinel-rich deposits seen by M^3, to place constraints on the origin and formation of these deposits. In addition these spectra will enlarge the dataset of "ground truth" objects for calibration and quantitative analysis for orbital remote sensing.

Experimental Technique:

Starting materials

The powdered starting materials (Table 2) were made from a mixture of oxides and synthetic gels, using procedures standard to the experimental petrology laboratory at NASA Johnson Space Center (JSC). The synthetic powders were fired and completely melted at 1 bar, quenched to homogeneous anhydrous glasses, and then ground to powder, remixed and stored in a desiccator to ensure that they remained anhydrous.

The starting composition AT-65785 (Table 2) was based on the reported bulk composition of Apollo pink spinel troctolite 65785 (Dowty et al. 1974). The starting composition A-81005 (Table 2) represents the average of the reported bulk compositions of ALHA81005 (Righter and Gruener 2013) and the compositions of nine glass spherules within ALHA81005.

1 bar Experiments

One-bar experiments were conducted in a 1 atm Deltech gas-mixing furnace in the laboratories of the ARES division at NASA Johnson Space Center (JSC). Oxygen fugacity was controlled by mixing CO-CO_2 gas to the desired fO_2 at or near 1 log unit below the iron-wüstite (IW) buffer. Oxygen fugacity was measured in a reference furnace through which exhaust gases from the experimental furnace were passed (Jurewicz et al. 1993). Temperature was measured using a $Pt_{94}Rh_6$-$Pt_{70}Rh_{30}$ thermocouple calibrated against the melting point of Au. Before the experimental runs, the starting mixture was mixed with poly-vinyl alcohol (PVA) and pasted onto rhenium-wire loops (rather than Pt) to minimize Fe loss (Borisov and Jones 1999). The experiments were undertaken in a procedure standard for this laboratory: the experimental charges were held above the liquidus at 1500ºC for 24 - 48 hours, lowered (1000ºC/hour) to the desired temperature, held at the desired temperature for 24 - 48 hours and then drop-quenched (< 5 seconds) into water.

Reflectance spectra

Reflectance spectra of the run products were collected at the RELAB spectroscopy facility at Brown University (Pieters 1983; Pieters and Hiroi 2004). The bidirectional VNIR reflectance spectra were measured at phase angles of i (incidence) = 30° and e (emergence) = 0° between 0.3 and 2.6 µm relative to halon at 5 nm intervals. The sieve fraction of each sample was <45 µm. The rhenium wire was taken out prior to the measurements. Mid-infrared measurements (up to 25 µm) were collected in biconical reflectance with the RELAB FT-IR spectrometer. VNIR reflectance spectra were analyzed with the Modified Gaussian Model (MGM), which enables deconvolution of an input spectrum into its component absorption features (Sunshine et al. 1990). An example MGM fit to an orthopyroxene spectrum (one of the simplest applications of the MGM; Fig. 9 suppl.) is provided in the supplemental material. A variety of MGM initial conditions were tested in order to evaluate the potential contributions of various phases (pyroxene, olivine, mafic glass, spinel). As MGM fits are purely mathematical solutions with no constraints from mineralogy (Fig. 10, suppl.), the solution chosen was that with the lowest error and which satisfied the physical conditions of the run product (i.e., the absorptions present in the fit were consistent with the mineralogy of the run product).

Analyses

Backscattered electron (BSE) images and quantitative chemical analyses were obtained with the Cameca SX100 electron microprobes (EMP) at NASA JSC and the American Museum of Natural History (AMNH). Quantitative analyses were obtained by wavelength dispersive spectrometry. Operating conditions were: 15kV accelerating voltage, 20nA beam current, focused electron beam (1 µm) for analyses of olivine, pyroxene and spinel, and defocused beam (5 µm) for analyses of plagioclase and glass. Peak and background counting times were 20-40 seconds per element. Analytical standards were well-characterized synthetic oxides and minerals including spinel (Mg, Al), chromite (Cr), diopside (Si), oligoclase (Na, Al), anorthite (Ca), hematite (Fe), forsterite (Si, Mg), fayalite (Fe), rutile (Ti), rhodochrosite (Mn), V_2O_3 (V), Co-metal (Co), ZnO (Zn), Ni-diopside (Ni), and orthoclase (K). Data quality was ensured by analyzing the standards as unknowns. After EMPA analyses of the experimental run products least squares mass balance calculations were performed in order to determine mineral abundances and to ensure that no phase was overlooked during microprobe analysis. The mass balance calculations were based in the major elements Si, Al, Ca, Mg, and Fe.

EXPERIMENTAL RESULTS

Experiments were conducted on both bulk compositions, at 1 bar, and temperatures between 1500°C and 1150°C. All experimentally produced minerals and glass compositions are homogenous. The experiments run at 1500 ºC contained only homogeneous glasses, which have the compositions intended from the starting materials (Table 2).

Were the Experiments at Equilibrium?

Crystallized phases in all experimental charges are chemically homogenous and no quench crystals are present in any experiment, suggesting that mineral-melt equilibria were approached. In the experiment at 1150ºC a fine grained intergrowth of olivine, pyroxene, and plagioclase (±glass) is found. To assess whether the experiments and therefore the crystallized phases were at chemical equilibrium, we calculated olivine-glass (liquid) equilibrium distribution-coefficients K_DFeO-MgO = $[XFeO_{(Ol)}XMgO_{(L)}]/[XMgO_{(Ol)}XFeO_{(L)}]$ for the 1300 ºC and 1250 ºC experiments and compared them to literature data believed to representing equilibria. K_D for all olivine/glass pairs (N = 5) fall within the expected range for equilibrium (0.31 for 1250 ºC and 0.30 for 1300 ºC) consistent with olivine-melt equilibrium (Roeder and Emslie 1970, Filiberto and Dasgupta 2011).

1 bar Experiments

AT – 65785: Experiments and crystallization sequence

Experiments on the composition AT-65785 yielded spinel on the liquidus at high temperatures. Run products included glass only, spinel + glass, spinel + plagioclase + glass, spinel + plagioclase + olivine + glass, and spinel + plagioclase + olivine ± pyroxene (Figs. 1 and 2). Compositional data for all phases and glasses are given in Table 3. Spinel is the liquidus phase first crystallizing between 1500 and 1450 ºC (Table 5). The abundance of spinel increases from ~3 wt% at 1450 ºC to ~8 wt% at 1300 ºC. Thereafter, it decreases to 4.5 wt% at 1150 ºC (Table 5). Figure 3 shows the changes in spinel chemistry with change in temperature for major (Fig. 3a) and minor elements (Fig. 3b). FeO increases with decreasing temperature and ranges from average 2.97 wt% FeO at 1450 ºC to an average of 5.25 wt% at 1150 ºC. The Mg# [molar Mg/(Mg+Fe)] decreases with decreasing temperature from ~0.94 to 0.89 while the Cr# $[Cr_2O_3/(Cr_2O_3+Al_2O_3)]$ increases from 0.027 at 1350 ºC to 0.031 at 1150 ºC. Plagioclase is the second phase to crystallize, coming on the liquidus between 1400 and 1350 ºC. The experiment at 1350 ºC contains 23.8 wt%

plagioclase and its abundance increases with decreasing temperature to 67.2 wt% at 1250 ºC (Tables 3, 5). Plagioclase is essentially pure anorthite, $An_{99.9}$, in all the experiments. Olivine starts to crystallize between above 1300 ºC. The experiment at 1300 ºC contains only 1.2 wt% olivine and its abundance increases with decreasing temperature to 13.3 wt% at 1250 ºC (Table 3, 5). Its Mg# decreases with decreasing temperature, from $Fo_{93.6}$ at 1300 ºC to Fo_{72} at 1150 ºC. The glass composition shows an increase in MgO, FeO, and SiO_2 with decreasing temperature, while Al_2O_3 shows a decrease consistent with crystallization of spinel and plagioclase (Fig. 4a). The minor elements that are concentrated in spinel (V, Ti, Cr) in the glass decrease with decreasing temperature and reach a minimum at 1300 ºC, after which they increase with decreasing temperature (Fig. 4b). This is consistent with the increase of spinel abundance with decreasing temperature to 1300 ºC followed by spinel decrease with decreasing temperatures.

The 1150 ºC experiment is at, or very close to, the solidus temperature of this composition. Near-solidus experiments are difficult to interpret, as they commonly have produce texturally inhomogeneous aggregates of phases (e.g., Dasgupta and Hirschman, 2007). In this case, the fine-grained aggregate consists of olivine-pyroxene-plagioclase ± melt. In these aggregates, individual grains are commonly less than 2 μm in diameter, thus too small to be analyzed by EMPA (see Fig. 1, 1150 ºC). However, in one area the grains were large enough so that one olivine analysis and one pyroxene analysis could be obtained. In order to get a general composition of the aggregate for mass balance calculations, it was analyzed with a broad beam (5-10 μm). Plagioclase and spinel crystallized slightly earlier and formed larger crystals. We did not get an analysis of the glass but based on mass balance it might be present in small proportions within the olivine-pyroxene-plagioclase aggregate texture.

A-81005: Experiments and crystallization sequence

Experiments on the composition A-81005 yielded plagioclase on the liquidus at high temperatures. Experimental run products included glass only, plagioclase + glass, and plagioclase + olivine + glass (Fig. 5). Compositional data for all phases and glasses are given in Table 4. Plagioclase comes onto the liquidus above 1400 ºC. At 1400 ºC about <1 wt% plagioclase has crystallized. This is an estimate based on mass balance calculations because no plagioclase was exposed in the cut section we examined. The abundance of plagioclase increases with decreasing temperature to 61 wt% at 1200 ºC (Fig. 6). It has a constant anorthite composition of $An_{99.9}$ in all the experiments. Olivine ($Fo_{83.6}$) only crystallizes at 1200 ºC with and abundance of 11.5 wt%. Spinel did not crystallize at any temperature from the A-81005 composition.

Reflectance spectra

Reflectance spectra of the AT-65785 experimental charges are shown in Fig. 7 (raw reflectance spectra are given in the supplemental material, Fig. 11). The 1500 ºC and 1450 ºC experimental runs (0 % crystals and 3% crystals respectively) exhibit spectral properties consistent with Fe-bearing glass; a broad absorption near 1 μm and a weaker absorption near 1.9 μm (Bell et al. 1976). Although the 1450 ºC charge does contain 3 wt% spinel, the characteristic spinel absorption at 2 μm is not apparent. All charges from runs at lower temperatures (>3% crystallinity) exhibit a prominent feature from spinel centered near 2 μm. At 1350 ºC (31.5% crystallinity) and 1300 ºC (48.7 % crystallinity), this feature can be attributed unambiguously to spinel, as the position and slope of the continuum is controlled by the glass. The spinel contribution to the 2 µm feature becomes more substantial (i.e., stronger, and more consistent with pure spinel) with decreasing temperature (and increasing crystallinity) and reaches a maximum at 1150 ºC (<5 wt% spinel; ~100 % crystallinity), despite the fact that the abundance of spinel decreases with decreasing temperature. Plagioclase started crystallizing at 1350 ºC (23.8 wt%) but its characteristic absorption feature around at ~1.25 µm (e.g., Adams and Goullad 1978) is not evident until perhaps at 1250 ºC, at which point 67 wt% plagioclase has crystallized (0.32 wt% FeO) and only 14 % of the experimental charge remains as glass. Olivine appears at 1300 ºC but its characteristic absorption near 1 µm is not apparent. This could be due to its low abundance (1.2 wt%), its high Mg# (Fo_{94}), and the strong glass band (51 % glass). At 1250 ºC (~86 % crystallinity) the reflectance spectrum clearly exhibits features in the 0.9-1.5 µm region associated with olivine (11.4 wt%) and perhaps plagioclase (65 wt%), both of which increase in strength (depth) in the 1150 ºC spectrum, which is essentially 100 % crystalline (Fig. 7).

The best-fit results from the MGM analyses are given in the supplemental material. Contributions from mafic silicates to the 2 µm absorptions could not be detected for any of the run products. While minor contributions are likely present for the products in which mafic silicates were more abundant (largely the lower-T products), these contributions were too weak to be distinguished above the background of the more prominent glass and spinel absorptions. No contribution from mafic silicates were observed in the glass-only or nearly glass-only products (1400°C and 1500°C), and the models are consistent with spectral characteristics of mafic glass (Bell et al. 1976), suggesting that the glass component is being modeled correctly. While a minor amount of spinel is present in the 1450°C sample, it did not produce a sufficiently substantial spectral signature to allow modeling of the specific spinel absorptions, perhaps due to its low abundance and low FeO content (the spinel in the 1450°C product had the lowest FeO content (~ 3 wt%; Table 3) of any spinel produced in this study).

For the products in which substantial crystalline material was present (T < 1400°C), a specific mafic glass component could not be modeled in the 2 μm region, because that region lacked sufficient structure to allow modeling of both the multi-component spinel feature and the weak ~2 μm glass feature. However, the glass absorption in that region does affect interpretation of the spinel absorption. The effect of glass on the 2 μm spinel absorption is illustrated in Figure 8, which plots the strength of the short-wavelength component of the spinel absorption against its center wavelength. This spinel absorption is composed of three absorption bands (Sunshine and Cloutis 1999), and the short-wavelength component of the absorption is stronger (relative to the long-wavelength component of the absorption) and falls at shorter wavelengths in the more glass-rich products (1300 °C and 1350 °C). This illustrates the effect of the mafic glass, which enhances the short wavelength component of the spinel absorption (it adds to the intensity) and "pulls" that short wavelength component of the spinel absorption to shorter wavelengths than observed for the more spinel-rich samples (the glass absorption is at shorter wavelengths, causing the composite "spinel + glass" feature to fall somewhere in between glass-dominated and spinel-dominated). For the samples in which less glass was present (1250°C and 1150°C), this contribution was not observed, likely due to the glass's lower modal abundance.

Reflectance spectra of the A81005 experimental run products have not yet been collected since the experiments did not crystallize any spinel. However, reflectance spectra of A81005 will be the measured in the future and presented elsewhere, to provide additional ground-truth data for orbital remote sensing.

DISCUSSION

The origin of the lunar spinel-bearing areas, exposing the so-called pink spinel anorthosite or PSA, is not yet resolved. Evidence from spectral reflectance studies has suggested that spinel in the PSA is very magnesian (Mg#'s ≥ 90, i.e., < 10 wt% FeO; Pieters et al. 2011; Dhingra et al. 2011; Jackson et al. 2012), and may be abundant at ~20-30 %vol of the rock (Pieters et al. 2011; Dhingra et al. 2011; Taylor and Pieters 2013). Further, the PSA is inferred to contain < 5%vol of mafic silicate minerals (olivine & pyroxene) and is thus composed mostly of plagioclase (or plagioclase-composition glass). These inferences suggest that formation of PSA requires an unusual, non-standard petrogenesis; and cannot be directly related to the ferroan anorthosite (FAN) of the Lunar Magma Ocean and crust (Taylor and Pieters 2013).

In this study we tested the hypothesis that the lunar spinel-rich materials are derived from impact melts of unusual composition and that they formed during low-pressure crystallization of (1) melts rich in olivine and plagioclase components, e.g., impact-melting lunar troctolite, and (2) melts of the average lunar crust, e.g., impact-melting average composition of the source region from which ALHA81005 originated. The experiments on A-81005 show that simply melting (e.g., during an impact event) and crystallizing a composition similar to ALHA81005's source region (bulk ALHA81005) does not yield spinel (Fig. 6). However, melting (e.g. during an impact event) and crystallizing a composition similar to Apollo pink spinel troctolite 65785 does yield spinel, up to ~8wt% (Fig. 2), somewhat more than was presented in the original Apollo sample. This proportion of spinel is significantly less than the suggested 20-30% spinel suggested to be in PSA. This difference in spinel proportions implies that, if PSA does contain 20-30% spinel, it could not have formed by simply melting of a common troctolitic composition similar to Apollo 65875 without some sort of process that would concentrate the crystallized spinel crystals, e.g., crystal settling due to gravity. In addition, at 1250 ºC (~86 % total crystallinity) ~13 wt% olivine (Fo_{88}) crystallized which resulted in a clear 1 μm absorption feature not seen in the PSA spectra. Thus, simply melting and crystallizing a typical troctolite composition, similar to Apollo sample 65785, cannot produce a rock with the optical properties of the PSA lithologies detected by M^3.

VNIR spectral reflectance analyses

The VNIR reflectance spectra of the experimental run products (Fig. 7a,b) provide a constraint on the composition and abundance of spinel in PSA. The strength of the spinel absorption near 2 μm increases monotonically as temperature decreases (Figure 7). The spectra of experimental products at 1250 ºC and at 1150 °C (~86 % crystallinity and 100% crystallinity, respectively) are, in fact, very similar in the 2 μm region (depth and position) to the M^3 spectra from PSA regions at Moscoviense basin (Fig. 7a ,b). The increase in 2 μm band depth is not a simple, linear effect of spinel abundance and composition (i.e., FeO content); spinel abundance is at its maximum in the 1300 ºC charge, and is lower in runs above and below that temperature. The FeO content of the spinel increases only slightly from ~3 wt% FeO at 1450 ºC to ~5 wt% at 1150 ºC. Instead, the 2 μm spinel feature appears to increases in strength (depth) with decreasing glass abundance to 1150 ºC (Fig.

8). Previous research indicates that the spinel 2 μm feature can become nearly saturated with as little as ~3-5 wt% FeO (Cloutis et al. 2004; Jackson et al. 2012), thus our experimental charges have sufficient FeO to produce very intense absorptions, and slight changes in spinel FeO content might not cause dramatic differences in the strength of the 2 μm absorption. The 2 μm features in the 1350 °C and 1450 °C spectra are consistent with a mixture of mafic glass and spinel (Fig. 9 suppl.), whereas the 2 μm features for the 1250 °C and 1150 °C spectra are quite consistent with mostly pure spinel (sensu stricto), and consistent with very little (14 wt% at 1250 ºC) to essentially no glass (at 1150 ºC). The spectra deviate slightly from those of pure spinel due to small proportions of olivine (1250 °C) and pyroxene (1150 °C); the pyroxene does not yield substantial spectral contributions in the 2 μm region, as spectra from the 1250 °C and 1150 °C charges are quite similar in that region. Thus, the increase in the 2 μm feature's strength, despite slight decreases in spinel abundance, is likely linked to the substantial decrease in glass abundance, as the spinel becomes the dominant mafic phase and the other variables (i.e., FeO content) that could cause appreciable changes in the reflectance properties, remain essentially constant. The effect of the glass on the 2 μm region is illustrated in Figure 8, which demonstrates the change in the short-wavelength component of the spinel absorption; that component falls at shorter wavelengths and becomes more intense for the higher-T, more glass-rich charges (1300 °C and 1350 °C).

The effect of space weathering

Our experiments do not (and cannot) evaluate the effects of space weathering, which may act to reduce the magnitude of the 2 μm spinel absorption feature of the PSA measured by M^3 (e.g., Noble et al. 2001; Hapke 2001; Pieters et al. 2000). In addition, the experimental run product at 1250 ºC (~86 % crystallinity) contains ~13 wt% olivine (Fo_{88}) which contributed to a clear 1 μm absorption feature. The spectra of the PSA lithologies detected by M^3 lack such a 1 μm absorption feature, which led to the conclusion that the PSA lithology contained little to no olivine or pyroxene (Pieters et al. 2011). Thus, a troctolitic starting composition similar to Apollo 65785 cannot directly produce the PSA lithology.

Nevertheless, our experiments have useful implications about the composition(s) and abundance(s) of spinel in the PSA lithology. Reflectance spectra near 2 μm of our low-T results for the AT-65785 composition, are very similar to the M^3 spectra of the PSA regions. The closest spectral match is with the 1150°C experiment, which is nearly completely crystalline and contains 4.5 wt% spinel. This similarity suggests that the spinel-rich PSA lithologies on the Moon might not be as spinel-rich as previously interpreted, and might contain as little as 4.5% spinel, or possibly less.

Our inference of relatively low spinel abundance in PSA is contingent on understanding the effects of space weathering, which tends to reduce the apparent depths of reflectance absorptions in the VNIR region. If space weathering affects spinel in this manner, our estimate of ~4.5% spinel in PSA is a minimum; further studies of space weathering are clearly needed.

IMPLICATIONS:

VNIR reflectance spectra analyses of our experimental run products are similar to the M^3 spectra of the lunar spinel-bearing areas, suggesting that our experimental spinels are similar in composition to those on the lunar surface. However, the shapes of the reflectance spectra in the 2 μm region also depend on the abundance and composition of coexisting crystalline phases and glass in the sample. The characteristic (depth and position) 2 μm spinel absorption features in the spectra of the experiments at 1250 ºC and especially at 1150 ºC are similar to the absorption feature of the PSA lithology at Moscoviense Basin on the lunar surface measured by M^3. The spinel in these experiments contains ~5 wt% FeO, confirming inference that spinel of the PSA most likely contains <10wt% FeO (Pieters et al. 2011). However, the abundance of spinel in the PSA could be far less than the 20-30% inferred by Pieters et al. (2011) and Dhingra et al. (2011); our 1250 ºC and 1150 ºC run products contain only ~5 wt% spinel, yet have reflectance spectra with a 2 μm spinel absorption feature that is comparable in depth and position to the spinel spectra observed by M^3 at Moscoviense basin (Fig. 7 a,b). Thus, the spinel-rich deposits detected by M^3 might not be as spinel-rich as previously thought and could contain as little as 5 wt% spinel. This is consistent with the spinel abundance found in spinel-bearing rocks (troctolites and cataclastites) from the Apollo and lunar meteorite sample collections (see Table 1) that typically contain from 5-6 wt% spinel (e.g., Dowty et al. 1974; Baker and Herzberg 1980; Ma et al. 1981; Marvin et al. 1989; Joy et al. 2012). However, the effect of space weathering on spinel-dominated material still needs to be explored as it could significantly weaken the 2 μm spinel absorptions in the PSA and thus indicate a greater modal abundance of spinel in these lithologies as compared to our laboratory measurements with similar 2 μm absorption strengths.

Acknowledgements: We are grateful to A. Peslier for assistance with the EMP analyses at NASA JSC. We thank Dr. Justin Filiberto for very helpful and fruitful discussions. We thank Dr. C. Pieters, Dr. S. Parman, and Mr. T. Prissel for helpful reviews and comments of this manuscript as well as Dr. R. Klima for handling this manuscript and extremely helpful thoughts and comments. Supported by NASA COS grant NNX13AF54G to J. Gross; LPI contribution *#1xxx*.

References:

Adams, J.B., and Goullaud, L.H. (1978) Plagioclase feldspars - Visible and near infrared diffuse reflectance spectra as applied to remote sensing. Proceedings of the 9th Lunar and Planetary Science Conference, 2901-2909.

Anderson, A.T. (1973) The texture and mineralogy of lunar peridotite, 15445,10. Journal of Geology, 81, 219–226.

Baker, M.B., and Herzberg, C.T. (1980) Spinel cataclasites in 15445 and 72435: Petrology and criteria for equilibrium. Proceedings of the 11th Lunar and Planetary Science Conference, 535-553.

Bell, P.M., Mao, H.K., and Weeks, R.A. (1976) Optical spectra and electron paramagnetic resonance of lunar and synthetic glasses - A study of the effects of controlled atmosphere, composition, and temperature, Proceedings of the 7th Lunar Science Conference, 2543-2559.

Bence, A.E., Delano, J.W. and Papike, J.J. (1974) Nature of the highland massifs at Tauris Littrow: an analysis of the 2-4mm soil fraction. Proceedings of the 5th Lunar Science Conference, 785-827.

Borisov, A., and Jones, J.H. (1999) An evaluation of Re as an alternative for Pt, for 1-bar loop technique: an experimental study at 1400°C. American Mineralogist 84, 1258–1534.

Cloutis, E. A., Sunshine, J. M., and Morris, R. V. (2004). Spectral reflectance-compositional properties of spinels and chromites: Implications for planetary remote sensing and geothermometry, Meteoritica and Planetary Sciences, 39, 545-565, doi:10.1111/j.1945-5100.2004.tb00918.x

Dasgupta, R., and Hirschmann, M.M. (2007) A modified iterative sandwich method for determination of near-solidus partial melt compositions. II. Application to determination of near-solidus melt compositions of carbonated peridotite. Contributions to Mineralogy and Petrology 154, 647-661.

Delano, J.W. (1977) Experimental melting relations of 63545, 76015 and 76055. Proceedings of the 8th Lunar Science Conference, 2097-2123.

Demidova, S.I., Nazarov, M.A., Lorenz, C.A., Kurat, G., Brandstätter, F., and Ntaflos, Th. (2007) Chemical composition of lunar meteorites and the lunar crust. Petrology, 15, 386-407.

Dhingra, D., Pieters, C.M., Boardman, J.W., Head, J.W., Isaacson, P.J., and Taylor, L.A. (2011) Compositional diversity at Theophilus Crater: Understanding the geological context of Mg-spinel bearing central peaks. Geophysical Research Letters, 38, L11201.

Dhingra, D., Pieters, C.M. Head, J.W. and Isaacson, P.J. (2013) Large mineralogically distinct impact melt feature at Copernicus crater – Evidence for retention of compositional heterogeneity. Geophysical Research Letters, 40, 1043-1048.

Dowty, E., Keil, K., and Prinz, M. (1974) Igneous rocks from Apollo 16 rake samples. Proceedings of the 5th Lunar Science Conference, 431-445.

Dymek, R.F., Albee, A.L., and Chodos, A.A. (1976) Petrology and origin of boulders #2 and #3, Apollo 17 station 2. Proceedings of the 7th Lunar Science Conference, 2325-2378.

Filiberto, J. and Dasgupta, R. (2011) Fe^{2+}-Mg partitioning between olivine and basaltic melts: Applications to genesis of olivine-phyric shergottites and conditions of melting in the Martian interior. Earth and Planetary Science Letters, 304, 527–537.

Finnila, A.B., Hess, P.C., and Rutherford, M.J. (1994) Assimilation by lunar mare basalts: Melting of crustal material and dissolution of anorthite, Journal of Geophysical Research, 99, 14677–14690.

Gross, J., and Treiman, A.H. (2011) Spinel-rich lithology in lunar meteorite ALHA81005: Origin and possible connection to M3 observations of the farside highlands. Journal of Geophysical Research, 116, E10009, *doi:10.1029/2011JE003858.*

Gross, J., Treiman, A.H, and Le, L. (2011) Unique spinel-rich lithology in lunar meteorite ALHA81005: Origin and possible connection to M3 observations of the farside highlands. 42nd Lunar and Planetary Science Conference, abstract # **2620**.

Hapke, B. (2001) Space weathering from Mercury to the asteroid belt. Journal of Geophysical Research, 106, 10039-10074.

Herzberg, C.T. (1978) The bearing of spinel-cataclasites on the crust-mantle structure of the moon. Proceedings of the 9th Lunar and Planetary Science Conference, 319-336.

Herzberg, C.T. (1983) The reaction forsterite + cordierite = aluminous orthopyroxene + spinel in the system $MgO-Al_2O_3-SiO_2$. Contributions to Mineralogy and Petrology, 84, 84-90.

Herzberg, C.T. and Baker, M.B. (1980) The cordierite- to spinel-cataclasite transition: Structure of the lunar crust. In Lunar Highlands Crust, vol. 1, pp. 113-132 (Papike J.J. and Merrill R.B. eds). Pergamon.

Hiroi, T., and Sasaki, S. (2001) Importance of space weathering simulation products in compositional modeling of asteroids: 349 Dembowska and 446 Aeternitas as examples. Meteoritics and Planetary Sciences, 36, 1587-1596.

Hurwitz, D.M., and Kring, D.A. (2013) Composition and structure of the South Pole - Aitken Basin impact melt sheet. *44th Lunar and Planetary Science Conference*, abstract #**2224**.

Isaacson, P., Nettles, J., Besse, S., Boardman, J., Cheek, L., Clark, R., Dhingra, D., Donaldson Hanna, K., Head, J., Klima, R., Kramer, G., Mall, U., Moriarty, D., Mustard, J., Petro, N., Pieters, C., Sunshine, J., Taylor, L., Tompkins, S., and Whitten, J. (2011) A Mineralogical survey of lunar crater central peaks with moon mineralogy mapper data: First results. 42nd Lunar and Planetary Science Conference, abstract #**2556**.

Jackson, C.R.M., Cheek, L.C., Parman, S.W., Cooper, R.F., and Pieters, C.M. (2012) Compositional constraints on lunar spinel anorthosite: synthesis of spinel with variable iron content. 43rd Lunar and Planetary Science Conference, abstract #**2335.**

James, O.B. (1980) Rocks of the early lunar crust, Proceedings of the 11th Lunar and Planetary Science Conference, 365-393.

Joy, K.H., Burgess, R., Hinton, R., Fernandes, V.A., Crawford, I.A., Kearsley, A.T., and Irving, A.J. (2011) Petrogenesis and Chronology of Lunar Meteorite Northwest Africa 4472: A KREEPy regolith breccia from the Moon. Geochimica et Cosmochimica Acta, 75, 2420-2452.

Jurewicz, A.J.G., Williams, R.J., Le, L., Wagstaff, J., Lofgren, G., Lanier, A., Carter, W., and Roshko, A. (1993) Technical Update: Johnson Space Center system using a solid electrolytic cell in a remote location to measure oxygen fugacities in CO/CO2 controlled-atmosphere furnaces. NASA Technical Memoradum 104774, National Aeronautics and Space Administration, 40.

Kaur, P., Chauhan, P., Bhattacharya, S., Kiran Kumar, A. and Kiran Kumar, A.S. (2012) Compositional diversity at Tycho crater: Mg-spinel exposures detected from Moon Mineralogy Mapper (M^3) data. 43rd Lunar and Planetary Science Conference, 1434.

Lal, D., Chauhan, P., Shah, R.D., Bhattacharya, S., Kiran, Kumar, A.S. and Kiran Kumar, A. (2012) Detection of Mg spinel lithologies on central peak of crater Theophilus using Moon Mineralogy Mapper (M3) data from Chandrayaan-1. Journal of Earth Systems Sciences, 121, 847-853.

Longhi, J. (1978) Pyroxene stability and the composition of the lunar magma ocean. Proceedings of the 9th Lunar and Planetary Science Conference, 285-306.

Longhi, J. and Boudreau, A.E. (1979) Complex igneous processes and the formation of the primitive lunar crustal rocks. Proceedings of the 10th Lunar and Planetary Science Conference, 2085-2105.

Ma, M.-S., Schmitt, R.A., Taylor, G.J., Warner, R.D., and Keil, K. (1981) Chemical and petrographic study of spinel troctolite in 67435: Implications for the origin of mg-rich plutonic rocks. Proceedings of the 12th Lunar Planetary Science conference**,** 640-642.

Marvin, U.B. and Walker, D. (1985) A transient heating event in the history of a highlands troctolite from Apollo 12 soil 12033. Proceedings of the 15th Lunar and

Planetary Science Conference, Part 2, Journal of Geophysical Research, 90, C421-C429.

Marvin, U.B., Carey, J.W., and Lindstrom, M.M. (1989) Cordierite-spinel troctolite, a new Mg-rich lithology from the lunar highlands. Science, 243, 925-928.

Morgan, Z., Liang, Y, and Hess, P. (2006) An experimental study of anorthosite dissolution in lunar picritic magmas: Implications for crustal assimilation processes. Geochimica et Cosmochimica Acta, 70, 3477-3491.

Noble, S.K., Pieters, C.M. Taylor, L.A. Morris, R.V. Allen, C.C. McKay, D.S. and Keller L.P. (2001) The optical properties of the finest fraction of lunar soil: Implications for space weathering. Meteoritics and Planetary Sciences, 36, 31-42.

Pieters, C.M. (1983) Strength of mineral absorption features in the transmitted component of near-infrared light: First results from RELAB. Journal of Geophysical Research, 88, 9534–9544.

Pieters, C.M. and Hiroi, T. (2004) Relab (Reflectance Experiment Laboratory): A NASA multiuser spectroscopy facility. 34th Lunar and Planetary Science Conference, 1720.

Pieters, C.M., Taylor, L.A. Noble, S.K. Keller, L.P. Hapke, B. Morris, R.V. Allen, C.C. McKay, D.S. and Wentworth, S. (2000): Space weathering on airless bodies: Resolving a mystery with lunar samples. Meteoritics and Planetary Sciences, 35, 1101-1107.

Pieters, C.M., Boardman, J., Buratti, B., Clark, R., Combe, J.P., Green, R., Goswami, J.N., Head, J.W. III, Hicks, M., Isaacson, P., Klima, R., Kramer, G., Kumar, K., Lundeen, S., Malaret, E., McCord, T.B., Mustard, J., Nettles, J., Petro, N., Runyon, C., Staid, M., Sunshine, J., Taylor, L.A., Thaisen, K., Tompkins, S., and Varanasi, P.

(2010) Identification of a new spinel-rich lunar rock type by the moon mineralogy mapper (M^3). 41st Lunar and Planetary Science Conference, 1854.

Pieters, C.M., Besse, S., Boardman, J., Buratti, B., Cheek, L., Clark, R.N., Combe, J.P., Dhingra, D., Goswami, J.N., Green, R.O.. Head, J.W., Isaacson, P., Klima, R., Kramer, G., Lundeen, S., Malaret, E., McCord, T., Mustard, J., Nettles, J., Petro, N., Runyon, C., Staid, M., Sunshine, J., Taylor, L.A., Thaisen, K., Tompkins, S., and Whitten, J. (2011) Mg-spinel lithology: a new rock-type on the lunar farside. Journal of Geophysical Research, Planets, 116, E00G08.

Pieters, C.M., Donaldson Hanna, K., Cheek, L., Dhingra, D., Moriarty, D., Parman, S., Jackson, C., Prissel, T., (2013) Compositional evolution of the early lunar crust: observed diverse mineralogy of the upper and lower crust. 44th Lunar and Planetary Science Conference, abstract #**2922**.

Prinz, M., Dowty, E., Keil, K., and Bunch, T.E. (1973) Spinel troctolite and anorthosite in Apollo 16 samples. Science, 179, 74-76.

Prissel, T.C., Parman, S.W., Jackson, C.R.M., Dhingra, D., Ganskow, G., Cheek, L.C., Rutherford, M.J., Hess, P., and Pieters, C.M. (2012) Melt-wallrock reactions on the Moon: Experimental constraints on the formation of newly discovered Mg-spinel anorthosites. 43rd Lunar and Planetary Science Conference, abstract #2743.

Prissel, T.C., Parman, S.W., Head, J.W., Jackson, C.R.M., Rutherford, M.J., Hess, P., Cheek, L.C., Dhingra, D., and Pieters, C.M. (2013) An “uncollected” member of the Mg-suite: Mg-Al pink spinel anorthosites and their place on the Moon. 44th Lunar and Planetary Science Conference, abstract #3066.

Righter K., and Gruener, J. (2013) Lunar Meteorite Sample Compendium. <http://curator.jsc.nasa.gov/antmet/lmc/index.cfm> Accessed July 2013.

Roeder, P.L. and Emslie, R.F. (1970) Olivine-liquid equilibrium. Contributions to Mineralogy and Petrology, 29, 275–289

Shearer, C.K., and Papike, J.J. (1999) Magmatic evolution of the Moon. American Mineralogist, 84, 1469-1494.

Snyder, G.A., Ruzicka, A., Taylor, L.A., and Patchen, A.D. (1998) Journey to the center of the regolith: A spinel troctolite and other clasts from drive tube 68001. 29th Lunar and Planetary Science Conference, 1144.

Snyder, G.A., Taylor, L.A., Patchen, A.D., Nazarov, M.A., and Semenova, T.S. (1999) Mineralogy and petrology of a primitive spinel troctolite and gabbros from Lunar 20, Eastern Highlands of the moon. 30*th* Lunar and Planetary Science Conference, 1491.

Sunshine, J.M., and Cloutis, E.A. (1999) Absorption Bands in Spinels: Comparisons of Laboratory and Asteroid Spectra. 30th Lunar and Planetary Science Conference, 1640.

Sunshine, J. M., and Pieters, C. M. (1998) Determining the composition of olivine from reflectance spectroscopy. Journal of Geophysical Research, 103, 13675-13688, doi:10.1029/98JE01217.

Sunshine, J.M., Pieters, C.M. and Pratt, S.F. (1990) Deconvolution of mineral absorption bands: An improved approach. Journal of Geophysical Research, 95, 6955-6966.

Sunshine, J.M., Besse, S., Petro, N.E., Pieters, C.M., Head, J.W., Taylor, L.A., Klima, R.L., Isaacson, P.J., Boardman, J.W., Clark, R.C. and the M3 Team (2010) Hidden in

Plain Sight: Spinel-Rich Deposits on the Nearside of the Moon as Revealed by Moon Mineralogy Mapper (M3). 41st Lunar and Planetary Science Conference, 1508.

Takeda, H., Yamaguchi, A., Bogard, D.D., Karouji, Y., Ebihara ,M., Ohtake, M., Saiki, K. and Arai, T. (2006) Magnesian anorthosites and a deep crustal rock from the farside crust of the moon. Earth and Planetary Science Letters, 247, 171–184.

Taylor, S.R. and Bence, A.E. (1975) Evolution of the lunar highland crust. Proceedings of the 6th Lunar Science Conference, 1121-1141.

Taylor, L.A. and Pieters, C.M. (2013) Pink-spinel anorthosite formation: Considerations for a feasible petrogenesis. 44th Lunar and Planetary Science Conference, 2785.

Treiman, A.H., Maloy, A.K., Shearer, C.K. Jr., and Gross, J. (2010) Magnesian anorthositic granulites in lunar meteorites in lunar meteorites Allan Hills 81005 and Dhofar 309: Geochemistry and global significance. Meteoritics and Planetary Science, 45, 163-180.

Vaughan, W.V., Head, J.W., Wilson, L., and Hess P.C. (2013) Geology and petrology of enormous volumes of impact melt on the Moon: A case study of the Orientale basin impact melt sea. Icarus 233, 749-765.

Walker, D. (1983) Lunar and terrestrial crust formation. Proceedings of the 14th Lunar Science Conference, Part 1. Journal of Geophysical Research, 88, B17-B25.

Walker, D., Grove, T.L., Longhi, J., Stolper, E.M., and Hays, J.F. (1973a) Origin of lunar feldspathic rocks. Earth and Planetary Science Letters, 20, 325-336.

Walker, D., Longhi, J., Grove, T.L., Stolper, E., and Hays, J.F (1973b) Experimental petrology and origin of rocks from the Descartes Highlands. Proceedings of the 4th Lunar Science Conference, 1013-1032.

Warner, R.D., Planner, H.N., Keil, K., Murali, A.V., Ma, M.-S., and Schmitt, R.A. (1976) Consortium investigation of breccia 67435. Proceedings of the 7th Lunar Science Conference, 2379-2402.

Wieczorek, M.A., Jolliff, B.L., Khan, A., Pritchard, M.E., Weiss, B.P., Williams, J.G., Hood, L.L., Righter, K., Neal, C.R., Shearer, C.K., McCallum, I.S., Tompkins, S., Hawke, B.R., Peterson, C., Gillis, J.J., and Bussey, B. (2006) The constitution and structure of the lunar interior. Reviews in Mineralogy and Geochemistry, 60, 221-364.

Yamada, M., Sasaki, S. Nagahara, H. Fujiwara, A. Hasegawa, S. Yano, H. Hiroi, T. Ohashi, H. and Otake, H. (1999) Simulation of space weathering of planet-forming materials: Nanosecond pulse laser irradiation and proton implantation on olivine and pyroxene samples. Earth Planets and Space, 51, 1255-1265.

Table and Figure captions

Figure 1: Back Scattered Electron (BSE) images of experimental run products of the experimental series AT-65785. Left hand side images show typical textures of experiments, right hand side are close-up images of the textures. Crystalline phases are: Ol, olivine; Plag, plagioclase; and Sp, spinel.

Figure 2: Variation in phase abundances (wt%) in the AT-65785 experiments at 1 bar as a function of temperature, showing the early crystallization of spinel at 1450 ºC and the late crystallization of olivine starting at 1350 ºC. *intergrowth = fine grained aggregate of olivine + pyroxene + plagioclase ± glass.

Figure 3: Changes in spinel compositions in the AT-65785 experiments with temperature. A) major elements; B) minor elements.

Figure 4: Changes in melt compositions in the AT-65785 experiments with temperature for major elements (A) and minor elements (B).

Figure 5: Back Scattered Electron (BSE) images of experimental run products of the experimental series A-81005, a) overall texture of 1200 ºC, b) close up of the texture. Crystalline phases are: Ol, olivine; and Plag, plagioclase.

Figure 6: Variation in phase abundances (wt%) in the A-81005 experiments at 1 bar as a function of temperature, showing the early crystallization of plagioclase at 1400 ºC. Spinel did not crystallize in any experiment.

Figure 7: Reflectance spectra of the AT-65785 experimental run products (1500 ºC to 1150 ºC, thick colored lines - dotted and solid) compared to M^3 spectra of spinel-rich deposit detected at Moscoviense basin (thin dotted black, grey, light grey lines) relative to featureless soil (Pieters et al., 2011). A) Reflectance spectra normalized to

1500 nm; B) Spectra normalized to the reflectance 'shoulder' between 1000 and 2000 nm (i.e., 1625 nm for 1500ºC/1450ºC experimental samples and 1420 nm for other experimental samples; 1250 nm for M^3 data) to facilitate comparison of the 2 µm absorption intensity. * = reflectance spectra of spinel-rich area at Moscoviense basin relative to featureless FS soil

Figure 8: Comparison of MGM-derived spectral properties for spinel-bearing samples. The 2 µm spinel feature is composed of three distinct absorptions (Sunshine and Cloutis, 1999), which were deconvolved in our spectra through MGM analyses (see supplemental material). The strength and position of the short wavelength (~1.8 µm) feature is illustrated, and demonstrates the influence of the mafic glass. The 1.8 µm absorption is both stronger (relative to the 2.6 µm feature) and at shorter wavelength for the more glass-rich samples (1350 °C and 1300 °C). The separation between the 1150 °C and 1250 °C in relative intensity (y axes) is likely a result of slight differences in modeled continuum slope between the two spectra. *Note that we use a glass abundance of 0 for the 1150 °C sample, although the sample does contain some glass in the "intergrowth"-like aggregates.

FIGURES:

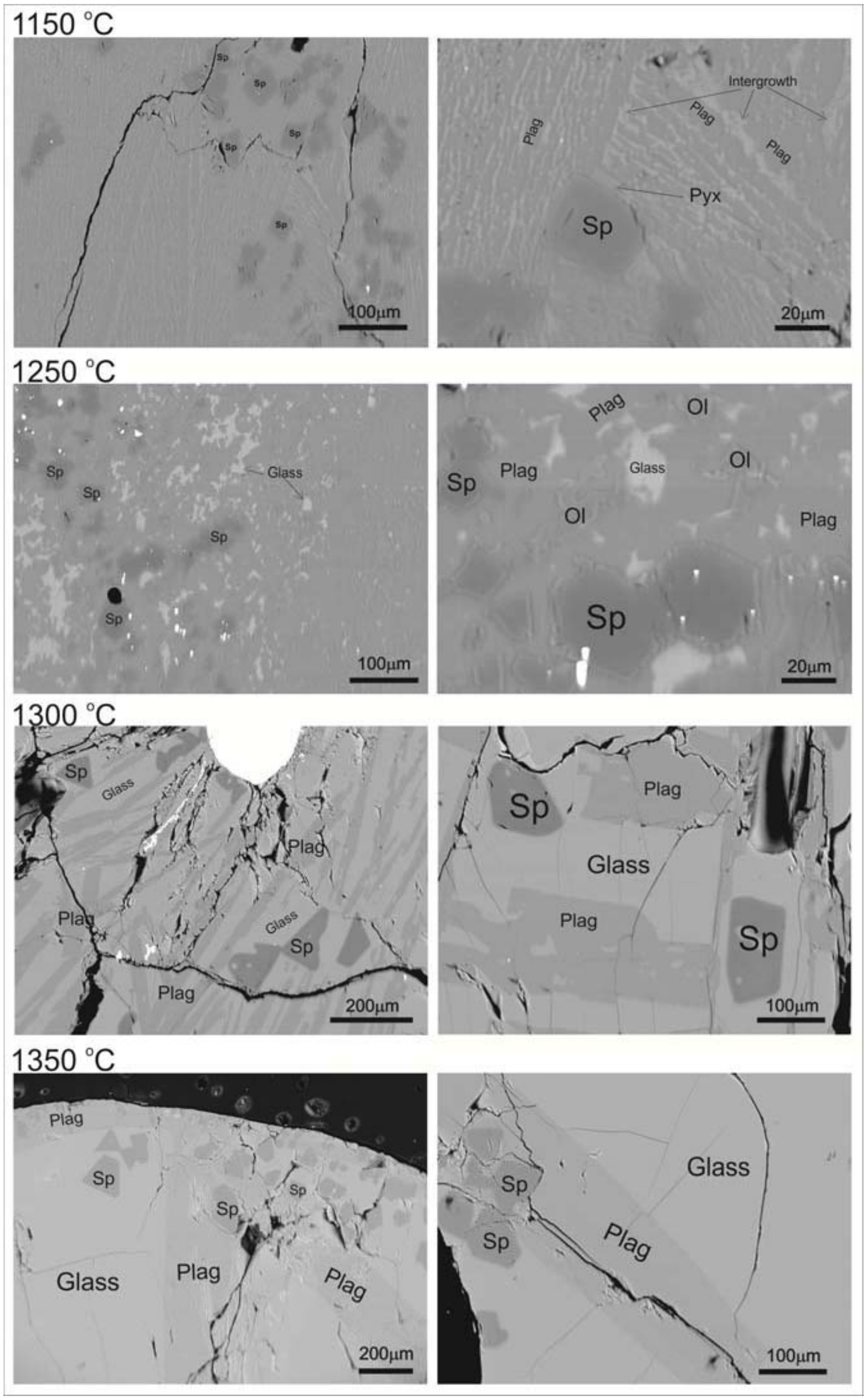

Figure 1: Back Scattered Electron (BSE) images of experimental run products of the experimental series AT-65785. Left hand side images show typical textures of

experiments, right hand side are close-up images of the textures. Crystalline phases are: Ol, olivine; Plag, plagioclase; and Sp, spinel.

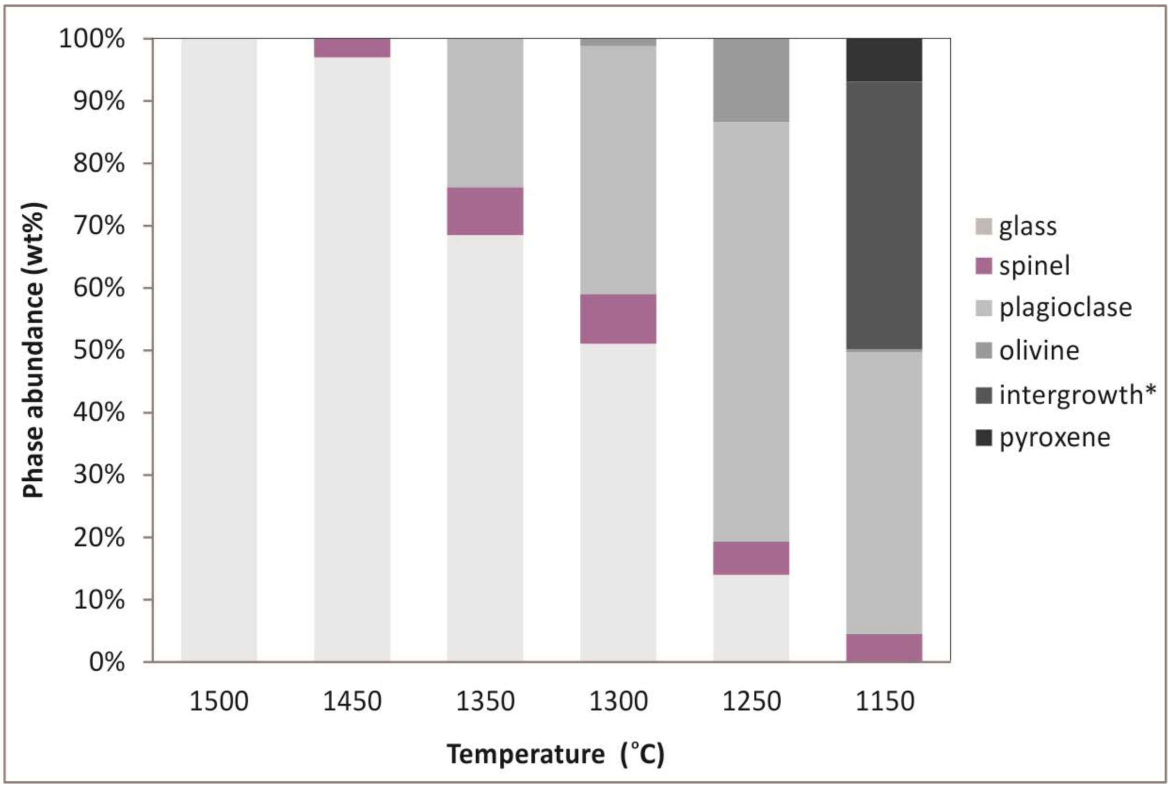

Figure 2: Variation in phase abundances (wt%) in the AT-65785 experiments at 1 bar as a function of temperature, showing the early crystallization of spinel at 1450 ºC and the late crystallization of olivine starting at 1350 ºC. *intergrowth = fine grained aggregate of olivine + pyroxene + plagioclase ± glass.

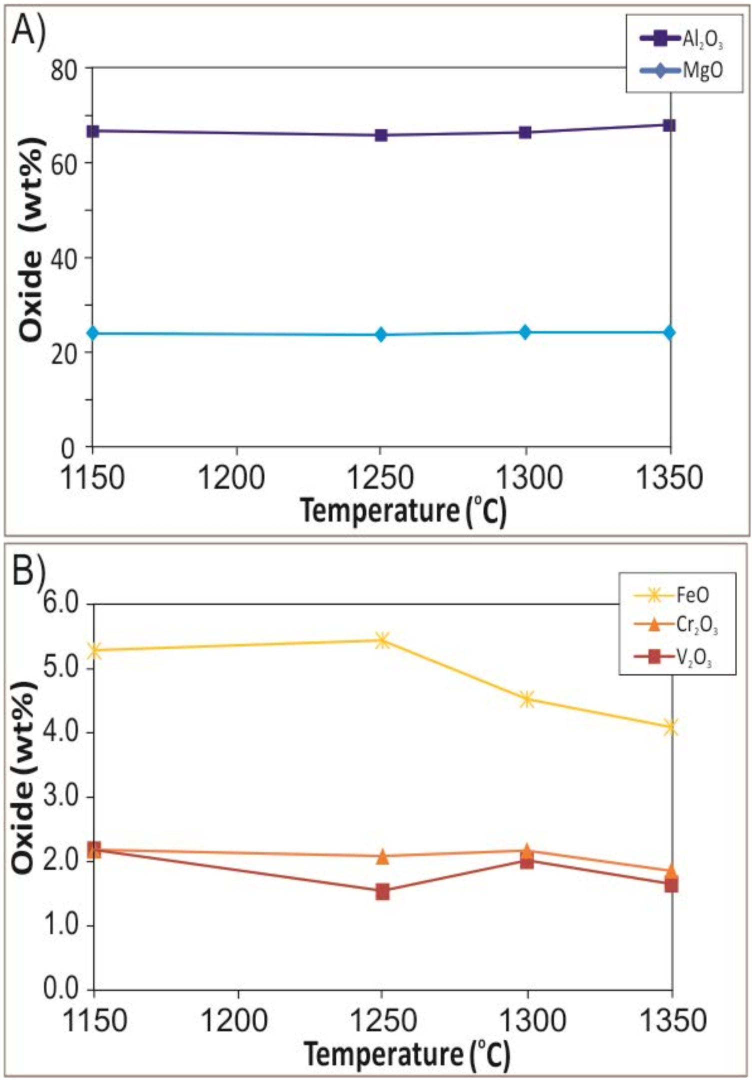

Figure 3: Changes in spinel compositions in the AT-65785 experiments with temperature. A) major elements; B) minor elements.

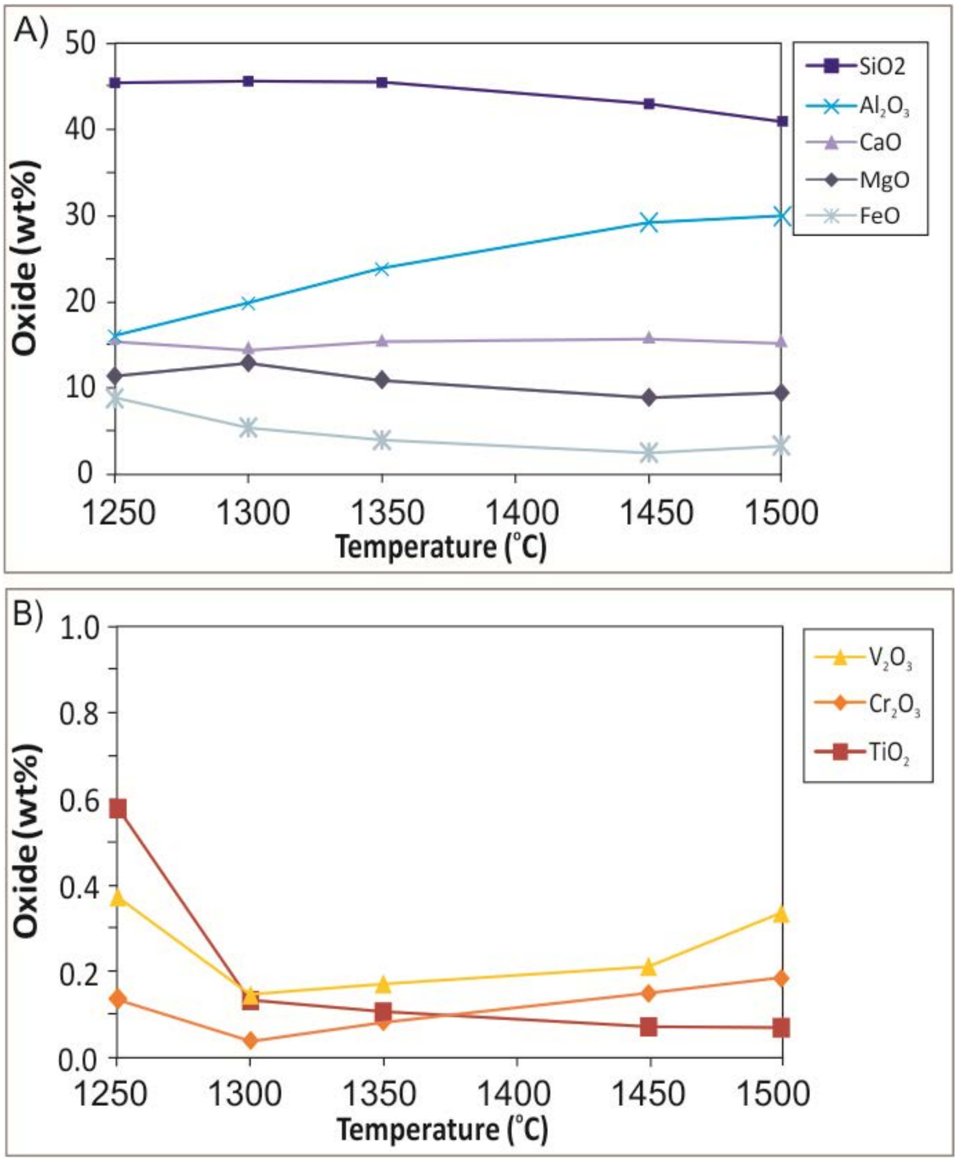

Figure 4: Changes in melt compositions in the AT-65785 experiments with temperature for major elements (A) and minor elements (B).

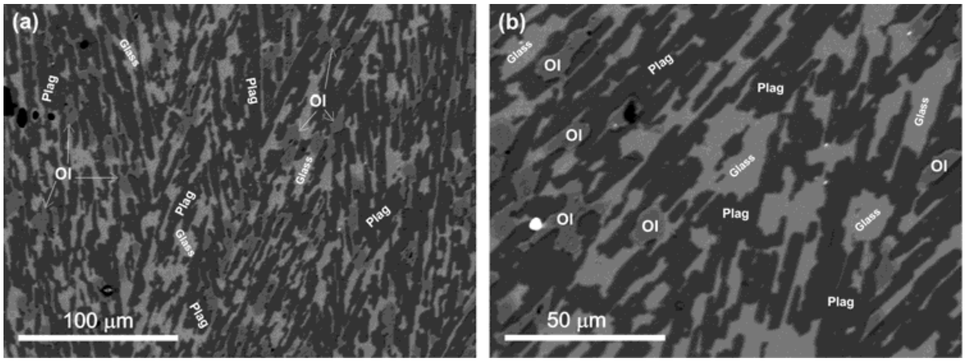

Fig. 5: Back Scattered Electron (BSE) images of experimental run products of the experimental series A-81005, a) overall texture of 1200 ºC, b) close up of the texture. Crystalline phases are: Ol, olivine; and Plag, plagioclase.

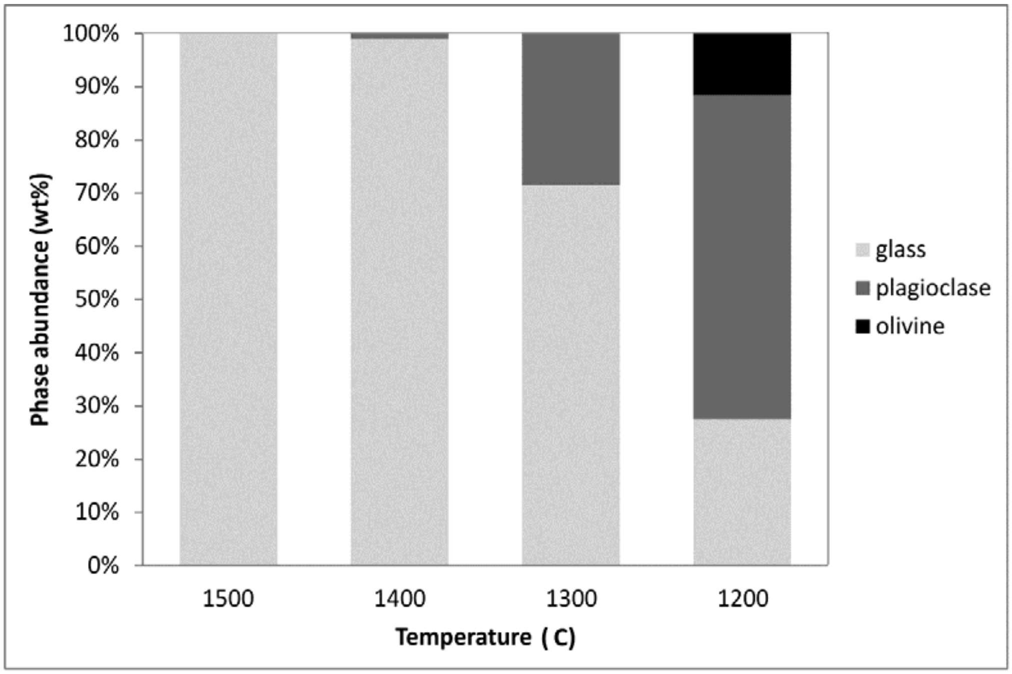

Figure 6: Variation in phase abundances (wt%) in the A-81005 experiments at 1 bar as a function of temperature, showing the early crystallization of plagioclase at 1400 ºC. Spinel did not crystallize in any experiment.

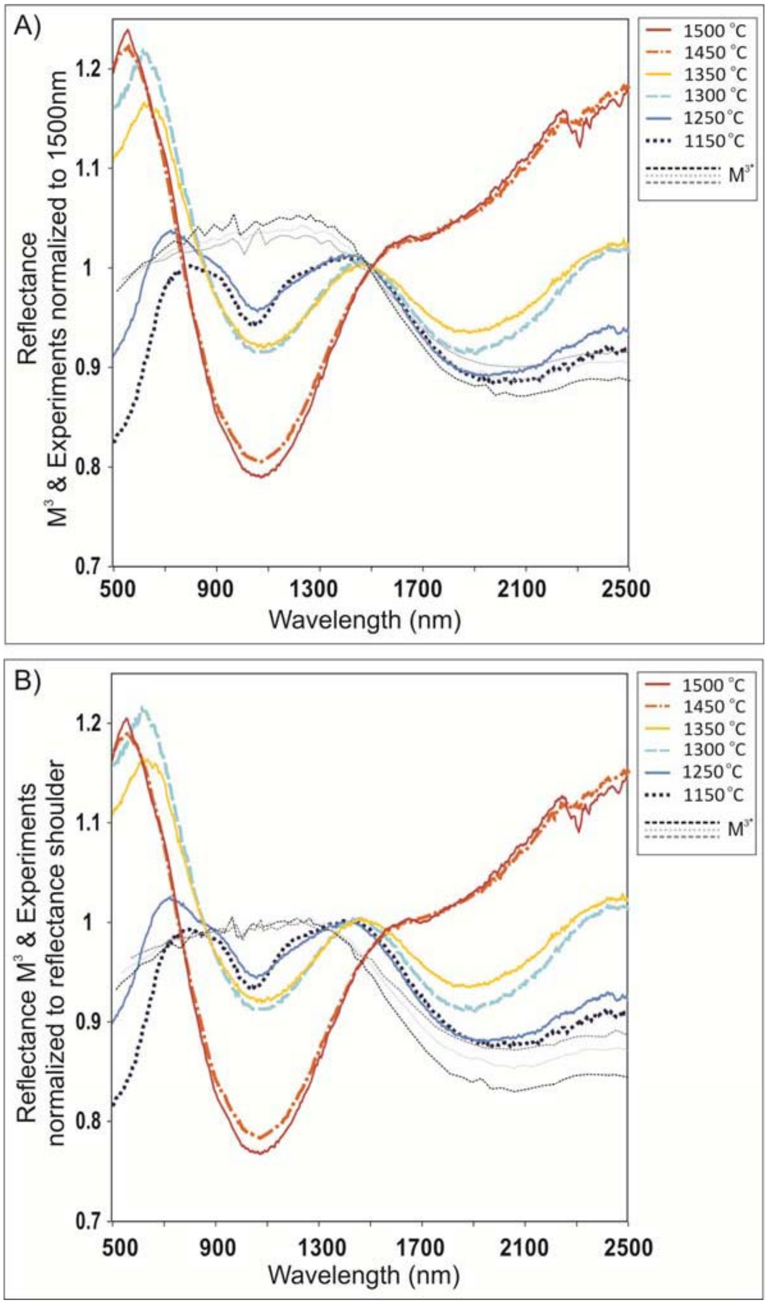

Figure 7: Reflectance spectra of the AT-65785 experimental run products (1500 ºC to 1150 ºC, thick colored lines - dotted and solid) compared to M3 spectra of spinel-rich deposit detected at Moscoviense basin (thin dotted black, grey, light grey lines) relative to featureless soil (Pieters et al., 2011). A) Reflectance spectra normalized to 1500 nm; B) Spectra normalized to the reflectance 'shoulder' between 1000 and

2000 nm (i.e., 1625 nm for 1500ºC/1450ºC experimental samples and 1420 nm for other experimental samples; 1250 nm for M3 data) to facilitate comparison of the 2 μm absorption intensity. * = reflectance spectra of spinel-rich area at Moscoviense basin relative to featureless FS soil.

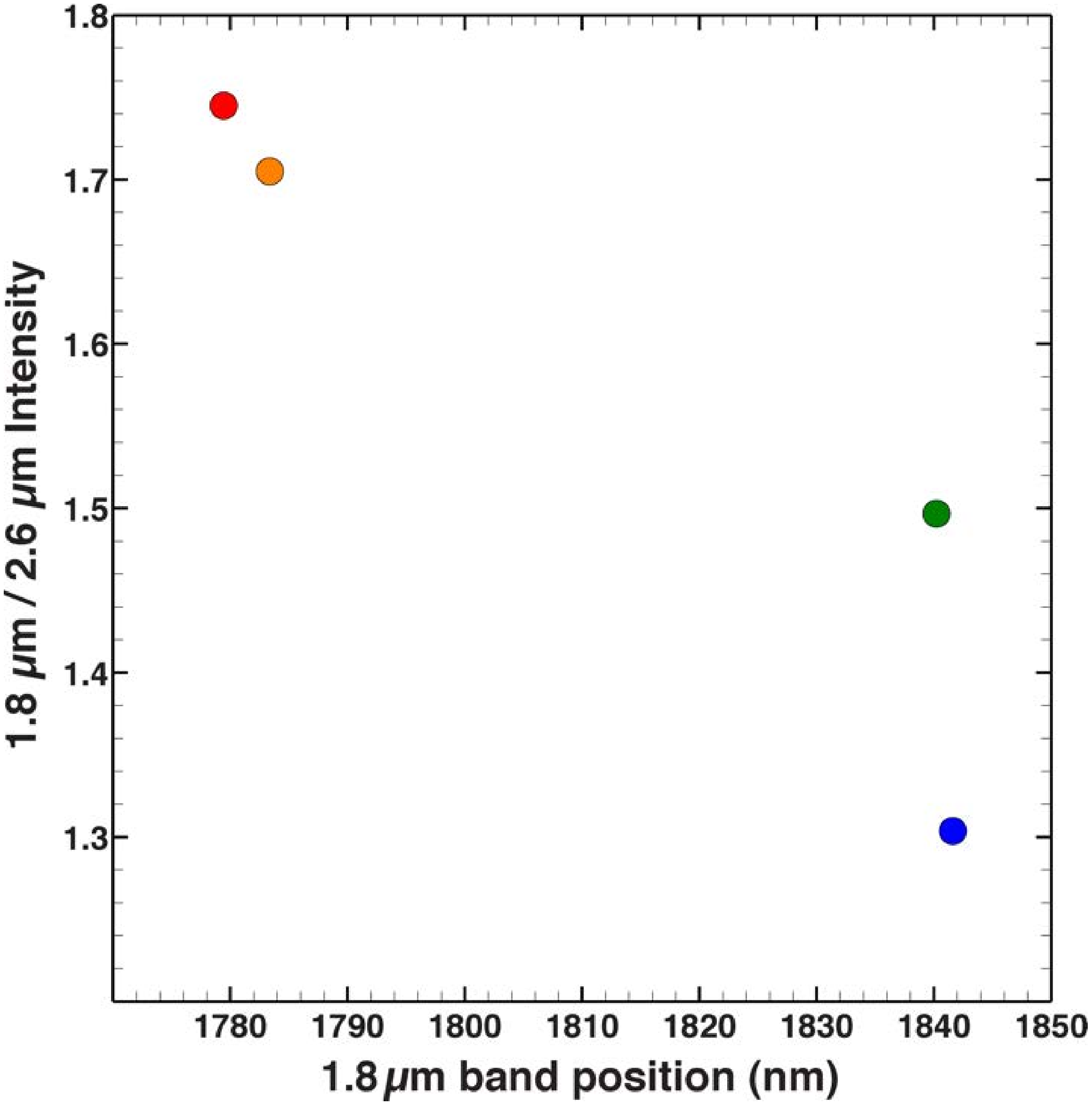

Figure 8: Comparison of MGM-derived spectral properties for spinel-bearing samples. The 2 μm spinel feature is composed of three distinct absorptions (Sunshine and Cloutis, 1999), which were deconvolved in our spectra through MGM analyses (see supplemental material). The strength and position of the short wavelength (~1.8 μm) feature is illustrated, and demonstrates the influence of the mafic glass. The 1.8 μm absorption is both stronger (relative to the 2.6 μm feature) and at shorter wavelength for the more glass-rich samples (1350 °C and 1300 °C). The separation between the 1150 °C and 1250 °C in relative intensity (y axes) is likely a result of slight differences in modeled continuum slope between the two spectra. *Note that we use a glass abundance of 0 for the 1150 °C sample, although the sample might contain some glass in the "intergrowth"-like aggregates.

Tables

Table 1: Lunar samples containing (Mg,Fe)-Al spinel.

Samples	%Spinel	Spinel composition		Suggested Origin	Author	Year
		Fe#	Cr#			
ALHA 81005,9	30	0.35	0.06	near/on surface	Gross&Treiman	2011
15295,101	6	0.21	0.18	30-50km	Marvin et al.	1989
65785	5	-	-	-	Dowty et al.	1974
67435,14	5	0.15	0.11	LMO cumulate	Prinz et al.	1973
67435,77	13	-	-	-	Ma et al.	1981
67435	5	-	-	on surface	Warner et al.	1976
73263	5-7	0.2-0.5	0.09	~60km	Bence et al.	1974
73263,1,11	-	-	-	≥ 12-32km	Baker&Herzberg	1980
72435,8	1-11	0.30-0.56	0.03-0.20	near surface	Baker&Herzberg	1980
72435,30 +,31	1-11	0.36-0.43	0.08-0.18	≥ 12-32km	Baker&Herzberg	1980
Dhofar 489	0.3	0.35	0.3	≥ 12-32km	Takeda et al.	2006
NWA 4472	8	0.33-0.45	0.1-0.22	-	Joy et al.	2012
15445;177	6-7	0.19-0.16	0.07-0.11	≥ 12-32km	Baker&Herzberg	1980
15445,10	-	0.2	0.14	~40km	Anderson	1973
62295	<1	0.1-0.24	-	melting of crust	Walker et al.	1973
68001/68002	1grain	0.35	0.077	40km	Snyder et al.	1998
72435	5	0.31-0.56	0.03-0.21	deep lower crust	Dymak et al.	1976
Luna 2003	-	0.08-0.09	0.03	lower crust	Snyder et al.	1999

LMO = Lunar Magma Ocean, Fe# = [molar Fe/(Fe+Mg)]; Cr# = [$Cr_2O_3/(Cr_2O_3+Al_2O_3)$].

Table 2: Experimental target and starting compositions.

	AT-65785		A-81005	
	material		material	
Wt%	target	Starting (N=42)	target	starting (N=43)
SiO_2	41.00	41.04 (±0.1)	44.7	44.98 (± 0.2)
TiO_2	0.07	0.07 (±0.02)	0.25	0.26 (±0.02)
Al_2O_3	29.80	29.97 (±0.1)	26.00	24.72 (±0.2)
Cr_2O_3	0.18	0.18 (±0.02)	0.12	0.11 (±0.02)
V_2O_3	0.15	0.33 (±0.07)	0.13	n.a.
MgO	9.50	9.39 (±0.07)	7.90	8.02 (±0.05)
CaO	14.80	15.67 (±0.1)	15.00	15.99 (±0.09)
MnO	0.15	0.19 (±0.02)	0.08	0.07 (±0.02)
FeO*	3.60	3.27 (±0.07)	5.50	5.09 (±0.08)
NiO	0.15	b.d.	0.10	b.d.
CoO	0.15	0.04 (±0.02)	-	-
Na_2O	0.26	b.d.	0.20	b.d.
K_2O	0.04	b.d.	0.02	b.d.
Total	100.00	100.18	100.00	99.35

b.d. = below detection limit; n.a. = not analysed; N = number of analyses

N = number of analyses; * = all iron assumed as FeO.

Table 3: Average composition of experimental run products AT-65785.

Oxides (wt%)	**1500 °C**	**1450 °C**		**1350 °C**			**1300 °C**			
	Glass (N=42)	**Glass (N=96)**	**Spinel (N=2)**	**glass**	**spinel**	**plagioclase**	**Glass (N=70)**	**Spinel (N=17)**	**Plagioclase (N=40)**	**Olivine (N=3)**
SiO_2	41.04 (±0.1)	43.03 (±0.2)	0.07 (±0.03)	45.52 (±0.6)	0.24 (±0.03)	44.03 (±0.4)	45.67 (±0.3)	0.12 (±0.04)	43.23 (±0.2)	42.27 (±0.2)
TiO_2	0.07 (±0.02)	0.07 (±0.1)	b.d.	0.11 (±0.02)	b.d.	b.d.	0.13 (±0.02)	0.02 (±0.02)	b.d.	b.d.
Al_2O_3	29.97 (±0.1)	29.26 (±0.1)	69.04 (±1.3)	23.81 (±0.4)	67.94 (±0.4)	36.44 (±0.1)	19.83 (±0.3)	66.41 (±0.9)	36.07 (±0.2)	0.10 (±0.02)
Cr_2O_3	0.18 (±0.02)	0.15 (±0.02)	1.96 (±0.03)	0.08 (±0.02)	1.86 (±0.1)	b.d.	0.04 (±0.2)	2.17 (±0.4)	b.d.	0.04 (0.01)
V_2O_3	0.33 (±0.07)	0.21 (±0.02)	1.41 (±0.06)	0.17 (±0.02)	1.65 (±0.2)	b.d.	0.14 (±0.02)	2.02 (±0.1)	b.d.	0.10 (±0.02)
MgO	9.39 (±0.07)	8.93 (±0.05)	25.45 (±0.8)	10.96 (±0.2)	24.21 (±0.3)	0.27 (±0.02)	12.96 (±0.1)	24.25 (±0.6)	0.21 (±0.05)	51.12 (±0.2)
CaO	15.67 (±0.1)	16.25 (±0.1)	0.10 (±0.01)	15.87 (±0.2)	0.08 (±0.02)	19.98 (±0.1)	14.96 (±0.1)	0.04 (±0.02)	19.94 (±0.1)	0.38 (±0.02)
MnO	0.19 (±0.02)	0.15 (±0.02)	0.09 (±0.02)	0.24 (±0.03)	0.14 (±0.03)	b.d.	0.28 (±0.03)	0.13 (±0.03)	b.d.	0.26 (±0.04)
FeO*	3.27 (±0.07)	2.48 (±0.06)	2.97 (±0.1)	3.95 (±0.1)	4.09 (±0.08)	0.08 (±0.04)	5.40 (±0.1)	4.52 (±0.05)	0.11 (±0.04)	6.28 (±0.1)
CoO	0.04 (±0.02)	b.d.	0.02 (±0.004)	0.02 (±0.02)	0.06 (±0.03)	b.d.	b.d.	0.04 (±0.02)	b.d.	0.03 (±0.01)
NiO	b.d.	b.d.	0.02 (±0.02)	b.d.	b.d.	b.d.	b.d.	b.d.	b.d.	b.d.
Na_2O	b.d.	b.d.	b.d.	b.d.	b.d.	b.d.	b.d.	b.d.	b.d.	b.d.
K2O	b.d.	b.d.	b.d.	b.d.	b.d.	b.d.	b.d.	b.d.	b.d.	b.d.
Total	100.18	100.58	101.15	100.77	100.32	100.89	99.45	99.76	99.66	100.62

b.d. = below detection limit; n.a. = not analysed; *intergrowth = fine grained aggregate of olivine, pyroxene, plagioclase (± glass); N = number of analyse; * = all iron assumed as FeO.

Table 3: Average composition of experimental run products AT-65785 (continued).

Oxides (wt%)	**1250 °C**				**1150 °C**				
	glass (N=93)	**spinel (N=60)**	**plagioclase (N = 108)**	**olivine (N=37)**	**intergrowth* (N=116)**	**spinel (N=88)**	**plagioclase (N=49)**	**olivine (N=3)**	**pyroxene (N=1)**
SiO_2	45.48 (±1.2)	0.09 (±0.1)	43.01 (±0.5)	40.92 (±0.8)	41.64 (±6.8)	0.10 (±0.9)	42.82 (±0.5)	37.80 (±0.3)	51.84
TiO_2	0.57 (±0.1)	0.02 (±0.1)	b.d.	0.02 (±0.02)	0.20 (±0.4)	0.02 (±0.02)	b.d.	0.08 (±0.04)	0.14
Al_2O_3	16.05 (±0.7)	66.04 (±0.8)	35.50 (±0.5)	0.29 (±0.2)	23.24 (±9.9)	66.71 (±0.8)	36.20 (±0.4)	1.17 (±0.4)	7.51
Cr_2O_3	0.13 (±0.03)	2.03 (±0.2)	b.d.	0.12 (±0.04)	0.25 (±0.3)	2.18 (±0.2)	b.d.	0.03 (±0.02)	0.14
V_2O_3	0.37 (±0.08)	1.48 (±0.2)	bd	0.29 (±0.09)	0.41 (±0.4)	1.61 (±0.4)	b.d.	0.04 (±0.02)	0.40
MgO	11.41 (±0.3)	23.67 (±0.8)	0.37 (±0.2)	46.77 (±0.9)	14.40 (±8.6)	24.11 (±0.6)	0.32 (±0.2)	34.34 (±0.2)	25.07
CaO	15.65 (±0.3)	0.06 (±0.1)	19.96 (±0.2)	0.67 (±0.1)	14.17 (±5.0)	0.07 (±0.03)	19.97 (±0.2)	1.46 (±0.3)	7.96
MnO	0.63 (±0.06)	0.19 (±0.1)	b.d.	0.63 (±0.06)	0.32 (±1.9)	0.19 (±0.04)	b.d.	1.10 (±0.02)	0.48
FeO*	8.82 (±0.8)	5.38 (±0.9)	0.32 (±0.2)	11.14 (±0.9)	5.48 (±3.5)	5.28 (±0.8)	0.22 (±0.06)	23.91 (±0.44)	6.44
CoO	0.04 (±0.02)	0.16 (±0.04)	b.d.	0.10 (±0.04)	0.07 (±0.2)	0.15 (±0.04)	b.d.	0.20 (±0.04)	0.08
NiO	b.d.	0.02 (±0.02)	b.d.	b.d.	b.d.	0.02 (±0.02)	b.d.	b.d.	b.d.
Na_2O	b.d.	b.d.	b.d.	b.d.	0.04 (±0.2)	b.d.	0.02 (±0.01)	b.d.	b.d.
K_2O	b.d.	b.d.	b.d.	b.d.	b.d.	b.d.	b.d.	b.d.	b.d.
Total	99.19	99.13	99.30	101.00	100.21	100.41	99.65	100.16	100.08

b.d. = below detection limit; n.a. = not analysed; *intergrowth = fine grained aggregate of olivine, pyroxene, plagioclase (± glass); N = number of analyse; * = all iron assumed as FeO.

Table 4: Average compositions of experimental run products A-81005.

Oxide (wt%)	**1500 ºC**	**1400 ºC**	**1300 ºC**		**1200 ºC**		
	glass (N=45)	Glass (N=5)	Glass (N=38)	Plagioclase (N=9)	Glass (N=35)	Plagioclase (N=2)	Olivine (N=17)
SiO_2	44.98 (± 0.2)	44.69 (± 0.07)	45.26 (±0.6)	43.49 (±0.3)	47.71 (± 0.5)	45.05 (± 0.9)	38.66 (± 0.4)
TiO_2	0.26 (±0.02)	0.27 (± 0.01)	0.40 (±0.03)	b.d.	0.87 (± 0.06)	b.d.	b.d.
Al_2O_3	24.72 (±0.2)	24.90 (± 0.07)	19.20 (±0.8)	35.43 (±0.3)	13.35 (± 1.1)	35.23 (± 0.1)	0.28 (± 0.2)
Cr_2O_3	0.11 (±0.02)	0.13 (± 0.03)	0.18 (±0.02)	b.d.	0.21 (± 0.02)	b.d.	0.18 (± 0.02)
V_2O3	n.a.	0.13 (± 0.01)	n.a.	b.d.	n.a.	n.a.	n.a.
MgO	8.02 (±0.05)	8.36 (± 0.05)	12.01 (±0.3)	0.38 (±0.06)	9.40 (± 0.4)	0.35 (± 0.06)	43.72 (± 0.5)
CaO	15.99 (±0.09)	16.67 (± 0.1)	14.09 (±0.2)	19.69 (±0.2)	14.12 (± 0.3)	19.40 (± 0.2)	0.59 (± 0.1)
MnO	0.07 (±0.02)	0.06 (± 0.02)	0.11 (±0.02)	b.d.	0.17 (± 0.02)	b.d.	0.18 (± 0.2)
FeO*	5.09 (±0.08)	2.90 (± 0.03)	7.61 (±0.2)	0.22 (±0.04)	10.70 (± 0.5)	0.54 (± 0.07)	15.32 (± 0.2)
Na_2O	b.d.	b.d.	0.02 (±0.02)	0.03 (±0.01)	b.d.	0.24 (± 0.02)	b.d.
K_2O	b.d.	b.d.	b.d.	b.d.	b.d.	b.d.	b.d.
Total	99.35	98.13	98.89	99.29	96.54	100.87	98.95

b.d. = below detection limit; n.a. = not analysed; N = number of analyses

N = number of analyses; * = all iron assumed as FeO.

Table 5: Phase abundance and crystallinity for each experiment with temperatures for compositions AT-65785 and A-81005.

Temperature (ºC)	**Phase abundances (wt%)**							**Crystallinity (%)**	**Mg#**		**KD**
AT-65785	glass	spinel	plagioclase	olivine	intergrowth*	pyroxene	Sum R^2		spinel	olivine	Ol-Liq
1500	100	0	0	0	0	0	0	0			
1450	97.0	2.99	0	0	0	0	0.71	3.0	93.9	-	
1350	68.5	7.7	23.8	0	0	0	0.18	31	91.3	-	
1300	50.9	8.0	39.6	1.2	0	0	0.01	49	90.5	93.6	0.31
1250	13.4	5.2	67.7	13.6	0	0	0.02	86	88.6	88.2	0.30
1150	0	4.5	45.1	0.5	42.7	6.9	0	100	89.1	71.9	-
A-81005											
1500	100	0	0	0	0	0	0	0	-	-	-
1400	>99	0	<1	0	0	0	0.7	<1	-	-	-
1300	65.7	0	34.3	0	0	0	0.02	34	-	-	-
1200	27.5	0	60.9	11.5	0	0	0.11	72	-	83.6	0.31

*intergrowth = fine grained aggregate of olivine, pyroxene, plagioclase (± glass).

Spinel and olivine Mg# and calculated KD (olivine-liquid) values where possible.